

## A transient backward erosion piping model based on laminar flow transport equations

Wewer, Manuel; Aguilar-López, Juan Pablo; Kok, Matthijs; Bogaard, Thom

**DOI**

[10.1016/j.compgeo.2020.103992](https://doi.org/10.1016/j.compgeo.2020.103992)

**Publication date**

2021

**Document Version**

Final published version

**Published in**

Computers and Geotechnics

**Citation (APA)**

Wewer, M., Aguilar-López, J. P., Kok, M., & Bogaard, T. (2021). A transient backward erosion piping model based on laminar flow transport equations. *Computers and Geotechnics*, 132, Article 103992. <https://doi.org/10.1016/j.compgeo.2020.103992>

**Important note**

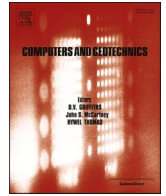
To cite this publication, please use the final published version (if applicable). Please check the document version above.

**Copyright**

Other than for strictly personal use, it is not permitted to download, forward or distribute the text or part of it, without the consent of the author(s) and/or copyright holder(s), unless the work is under an open content license such as Creative Commons.

**Takedown policy**

Please contact us and provide details if you believe this document breaches copyrights. We will remove access to the work immediately and investigate your claim.



## Research Paper

# A transient backward erosion piping model based on laminar flow transport equations

Manuel Wewer<sup>a,c</sup>, Juan Pablo Aguilar-López<sup>a,b,\*</sup>, Matthijs Kok<sup>a</sup>, Thom Bogaard<sup>b</sup>

<sup>a</sup> Hydraulic Engineering, Faculty of Civil Engineering and Geosciences, Delft University of Technology, P.O.Box 5048, 2600 GA Delft, the Netherlands

<sup>b</sup> Water Management, Faculty of Civil Engineering and Geosciences, Delft University of Technology, P.O. Box 5048, 2600 GA Delft, The Netherlands

<sup>c</sup> Hydraulic Engineering and Technical Hydrodynamics, Faculty of Civil Engineering, TU Dresden, IWD, 01062 Dresden, Germany

## ARTICLE INFO

## Keywords:

Backward erosion piping (BEP)  
Exner's equation  
Transient flow  
Finite elements

## ABSTRACT

Backward erosion piping is an internal erosion process, which compromises the stability of water retaining structures such as dams and levees. In this paper, we propose a numerical solution that combines a 2D Darcy groundwater solution with Exner's 1D sediment transport mass conservation equation. As an estimate of sediment transport, we tested four different empirical transport equations for laminar flow. The model performance was evaluated based on the results of the real-scale IJkdijk experiment. Through this, we were able to demonstrate the applicability of existing sediment transport equations to the description of particle motion during piping erosion. The proposed transient piping model not only predicts the pipe progression in time, it also allows for an identification of pore pressure transitions due to the erosion process. A major conclusion of the study is that from the four different modeling approaches for laminar flow, it is recommended to follow the approach of Yalin et al. regarding the simulation of backward erosion piping for dike configurations similar to those of the IJkdijk experiment.

## 1. Introduction

Backward erosion piping (BEP) has been proven to be one of the main failure mechanisms of water-retaining structures worldwide (Danka and Zhang, 2015). Dikes, which are often built on sandy aquifers, are particularly vulnerable to this special type of internal erosion (Van Esch et al., 2013). Since BEP represents a major threat to dike stability, a great interest in the Dutch flood protection system has emerged in understanding and describing this process. In the event of flooding, seepage forces at the unfiltered downstream exit initiate BEP and the erosion progresses towards the upstream side at the interface between the cohesive dike material and the cohesionless aquifer. Dendrite cavities form and progress underneath the dike while the eroded material is transported towards the piping outlet, where it stacks in the form of sand boils. Once the erosion reaches the upstream side, the created pipes will widen rapidly until the dike loses its stability and collapses.

BEP has been studied by different scientists (Bligh, 1910; Griffith, 1914; Lane, 1935; Terzaghi et al., 1996; De Wit et al., 1981; Hanses, 1985; Müller-Kirchenbauer et al., 1993; Qiu-ling et al., 2007; El Shamy

and Aydin, 2008; De Vries et al., 2010; Schmertmann, 2000; Ojha et al., 2003; Sellmeijer, 1988; Sellmeijer et al., 2011; Wang et al., 2014; Jianhua, 1998; Bersan et al., 2013; Vandenboer et al., 2013; Robbins, 2016; Aguilar-López et al., 2018; Lominé et al., 2013; Tran et al., 2017; Sellmeijer and Koenders, 1991; Lachouette et al., 2008; Fujisawa et al., 2010; Zhou et al., 2012; Rotunno et al., 2019) for more than a century. The first prediction models aimed to determine the hydraulic head and hydraulic gradient as erosion criteria (Bligh, 1910; Griffith, 1914; Lane, 1935; Terzaghi et al., 1996). However, these models only roughly cover the actual erosion process. In order to get a better understanding of BEP, numerous multiscale experiments were conducted in the last decades (De Wit et al., 1981; Hanses, 1985; Müller-Kirchenbauer et al., 1993; Qiu-ling et al., 2007; El Shamy and Aydin, 2008; De Vries et al., 2010). Analytical models have been developed based on these observations or using a purely theoretical approach (Schmertmann, 2000; Ojha et al., 2003; Sellmeijer, 1988; Sellmeijer et al., 2011). In addition to the development of experimental and analytical models, methods for the numerical simulation of the piping process were introduced.

According to Wang et al. (2014), these numerical piping models can be categorized into three groups. The first group includes models

\* Corresponding author at: Hydraulic Engineering, Faculty of Civil Engineering and Geosciences, Delft University of Technology, P.O.Box 5048, 2600 GA Delft, the Netherlands.

E-mail address: [j.p.aguilarlopez@tudelft.nl](mailto:j.p.aguilarlopez@tudelft.nl) (J.P. Aguilar-López).

<https://doi.org/10.1016/j.compgeo.2020.103992>

Received 24 March 2020; Received in revised form 4 December 2020; Accepted 28 December 2020

Available online 1 February 2021

0266-352X/© 2021 The Authors.

Published by Elsevier Ltd.

This is an open access article under the CC BY-NC-ND license

(<http://creativecommons.org/licenses/by-nc-nd/4.0/>).

representing the piping zone as a porous medium of extremely high permeability instead of a fluid flowing conduit (Jianhua, 1998; Bersan et al., 2013; Vandenboer et al., 2013; Robbins, 2016; Aguilar-López et al., 2018). This solution is based on the assumption that flow inside the erosion channel is laminar, which has been confirmed by recent laboratory tests (van Beek et al., 2019). Consequently, the cubic law can be applied for estimating the approximated hydraulic conductivity inside the eroded channel (Snow, 1965). A common characteristic of the first group of piping models is the non-consideration of particle transport rates, making it impossible to estimate the progression of the erosion in time and space. However, to understand the temporal development of the internal erosion and to simulate the time required for the pipe to progress, the inclusion of the transient particle transport behavior is of great importance. The models in the second group simulate the water and soil particles at a microscale, using the Discrete Element Method (DEM). The fluid inside the pipe is idealized by Navier–Stokes equations, coupled with a Darcy seepage solution. The individual modeling of the particles delivers a detailed description of the whole process and shows promising results of capturing the erosion process (El Shamy and Aydin, 2008; Lominé et al., 2013; Tran et al., 2017). In the third group of models, the geometry is separated into phases representing the soil skeleton, the fine particles and the pore water. The division of the geometry into these phases may differ between different authors (Wang et al., 2014; Sellmeijer and Koenders, 1991; Lachouette et al., 2008; Fujisawa et al., 2010; Zhou et al., 2012; Rotunno et al., 2019). The models included in the third group are the most common approaches in piping research. In addition to these three model categories, there are hybrid simulation approaches, such as the coupled continuum-discrete model for saturated granular soil, which models fluid motion based on Navier–Stokes equations and applies the DEM to simulate the microscale deposition of solid particles (El Shamy and Zeghal, 2005).

All of the above-mentioned piping models are able to simulate the main characteristics of BEP. However, the models of the second and third group are computationally very expensive and unpractical for engineering applications (Robbins, 2016). In the present study we propose a numerical solution which allows to simulate specific piping features, like the erosion evolution over time, while remaining categorized in the first group of models. In order to include the time component of the erosion process, the proposed numerical piping model applies existing sediment transport equations explicitly for laminar flow to the time-dependent seepage equations. This process describes the initial development of an erosion channel and its progression until reaching and breaking through to the water reservoir.

The proposed finite element model is based on a continuous approach, which describes the erosion process via laminar flow transport equations and Exner's sediment mass conservation equation. This continuum-based modeling is considered more practical for large-scale applications than a discrete modeling of the erosion process. Similar approaches to study sand erosion, which did not all explicitly investigate BEP, also applied a continuum-based modeling approach to describe the internal erosion process in form of preferential pathways (Papamichos and Vardoulakis, 2005; Stavropoulou et al., 1998; Muhlhaus et al., 2015; Zhang et al., 2013; Bui et al., 2019).

In the following, this paper will first provide a description of the modeling method. Subsequently, Section 3 contains an application example consisting of a comparison between the formulated numerical solution and the real-scale IJkdijk model with its experimental observations. The results of the transient piping model are assessed and discussed in Section 4, followed by the conclusion of the study.

## 2. Method

The method proposed in the current paper consists of building a 2D finite element model in COMSOL Multiphysics (AB, 2019). The numerical BEP model will allow for the simulation of the temporal piping

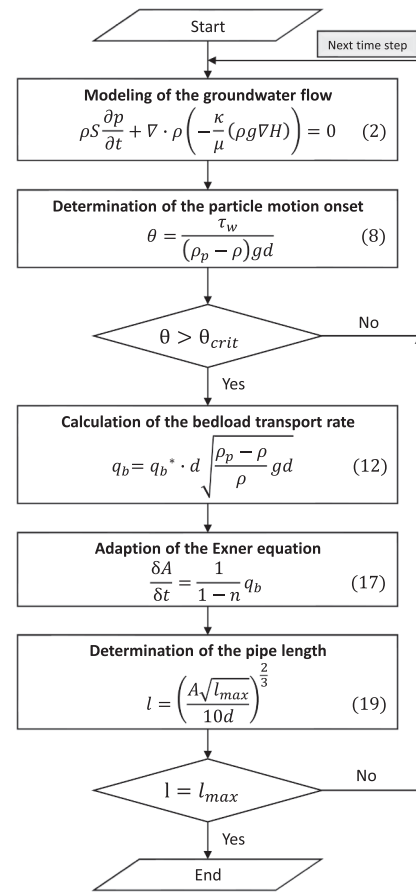


Fig. 1. Methodology flow chart.

process. In this, the pipe progression can be reproduced until the pipe penetrates into the upstream water reservoir, however, the following pipe widening, and dike failure will not be simulated within the proposed piping model. The methodology flow chart in Fig. 1 summarizes the calculation steps of the pipe progression. The description of the individual numerical operations follows below.

### 2.1. Governing flow equations

Groundwater flow in saturated porous media is generally modeled using Darcy's law. The Darcy velocity  $u$  can be written as

$$u = -\frac{\kappa}{\mu}(\rho_f g \nabla H) \quad (1)$$

in which  $\kappa$  denotes the intrinsic permeability,  $\mu$  the dynamic viscosity,  $\rho_f$  the fluid density,  $g$  the gravitational acceleration and  $\nabla H$  the hydraulic gradient.

In addition to Darcy's law, the proposed numerical simulation also accounts for the conservation of mass. In case of time-dependent problems, the equation of fluid continuity is expressed as

$$\rho_f S \frac{\partial p}{\partial t} + \nabla \cdot (\rho_f u) = 0 \quad (2)$$

in which  $S$  represents the storage and  $p$  the pore pressure. The storage capacity of the aquifer itself depends on the soil porosity  $n$ , the compressibility of the pore fluid  $\chi_f$ , and the compressibility of the soil matrix  $\chi_p$ :

$$S = n\chi_f + (1-n)\chi_p \quad (3)$$

The piping erosion progression is also controlled by the fluid flux inside

the erosion channel. In the proposed numerical solution, the piping-eroded zone will be represented as a highly permeable porous media. This approach is based on the assumption that during the piping process, laminar flow is always present inside the pipe, which enables the application of the Hagen-Poiseuille equation:

$$U = -\frac{2D_h^2}{\alpha\mu}(\rho_f g \nabla H) \tag{4}$$

In this equation,  $U$  represents the mean velocity inside the pipe,  $D_h$  the hydraulic diameter and  $\alpha$  an adjustment factor. The Darcy velocity  $u$  and the Hagen-Poiseuille velocity  $U$ , each represent a cross-section averaged discharge. Assuming that the flux inside the pipe is equivalent to the flux inside a porous media, one concludes that Hagen-Poiseuille flow can be described as Darcy flow by applying the cubic law. The fictitious permeability of the channel  $\kappa^*$  required for Darcy's law results in:

$$\kappa^* = \frac{2D_h^2}{\alpha} \tag{5}$$

The hydraulic diameter  $D_h = 4A/P$  is derived from the cross-section  $A$  and the perimeter  $P$  of the piping channel. For the piping erosion channel, an infinitely wide pipe is assumed for which the hydraulic diameter equals twice the pipe height. Aguilar-López et al. (2018) showed that under steady state conditions for different cross-sections sufficient head loss inside the cavity may not be achieved. Van Beek (2015) also acknowledged that while an infinitely wide channel (parallel plates) was a good approximation for the flux inside small channels with ratios of depth to width of 0.1, it tended to overestimate the flow rate for channels with larger ratios. Our main reasoning for this over-estimation originates from the assumption that the erosion channels can be represented as smooth, straight-lined, and uniform channels. Several authors (Elsworth and Goodman, 1986; Cook et al., 1990; Ge, 1997; Xiao et al., 2013; Wang et al., 2015; Li et al., 2019) who have investigated the validity of the cubic law in fractures, have proposed different rationales behind cubic law adjustment factors. Our  $\alpha$  adjustment factor is defined by the geometry of the cavity, its sinuosity, and its cross-section variation; factors which were not included in the studies conducted by Aguilar-López et al. (2018) and Van Beek (2015). We define the  $\alpha$  factor as the product of three different frictional effects ( $\beta$ ,  $T_h$  and  $f$ ) that will eventually reduce the estimated fictitious permeability  $\kappa^*$ . This is due to the fact that the eroded channel significantly differs from the idealized smooth, straight, and parallel-plated channel model. The proposed  $\alpha$  adjustment factor can be expressed as

$$\alpha = \beta T_h f \tag{6}$$

where  $\beta$  is a geometric cross-section factor,  $T_h$  is the hydraulic tortuosity factor and  $f$  is a cross-section variation factor (Muzychka and Yovanovich, 2009). The first factor  $\beta$  aims to correct the flux reduction as there are frictional losses originating from the idealistic cross-section assumption. In the specific case of laminar flow between infinitely wide parallel plates, the geometrical cross-section correction factor  $\beta = 96$  (Muzychka and Yovanovich, 2009). The second correction term  $T_h$  is also referred to as the hydraulic tortuosity correction factor (Bear, 1975) and aims to correct the fact that the erosion channel is a meandering and branching one instead of being a straight-lined pipe. The geometric tortuosity indicates the degree of torsion of transport paths inside the subsoil (Ghanbarian et al., 2013), which is expressed as the ratio between the actual pipe length  $L_g$  and the straight line between the pipe ends  $L_s$ . The hydraulic tortuosity  $T_h$  corresponds to the square of the geometric tortuosity, since the latter takes shortcuts that cross streamlines (Clenell, 1997) and it is expressed as:

$$T_h = \left(\frac{L_g}{L_s}\right)^2 \tag{7}$$

The classical cubic law overestimates the flow through small channels,

**Table 1**  
Expressions for the critical Shields parameter in laminar flow.

Authors	Critical Shields Parameter
Yalin and Karahan (1979)	$\theta_c$ from Shields diagram
Cheng (2004)	$\theta_c = 0.147d_*^{-0.29}$
Charru et al. (2004)	$\theta_c = 0.12$
Ouriemi et al. (2009)	$\theta_c = \mu \frac{1-n}{2}$

not only because of the geometrical cross-section correction factor or the hydraulic tortuosity but also because of the impact of channel cross-section variations (Witherspoon et al., 1980; Elsworth and Goodman, 1986; Wang et al., 2015). Due to its simplicity, our model introduces the fracture surface characteristic factor  $f$  proposed by Witherspoon et al. (1980). This factor compensates for the deviations from the ideal concept of parallel plates along the channel and takes into account narrowing and widening of the conduit. Both tortuosity and cross-section variation can be observed in Figs. 8 and 9 included in Appendix A, in which previous piping erosion experiments are presented. Witherspoon et al. (1980) deduced the  $f$  factor from the energy losses derived from acceleration and deceleration of the fluid due to the diverging and converging flow lines. They originate from the reduction and expansion of the cross-section. Witherspoon et al. concluded that the energy losses did not depend on the studied rock materials themselves but rather on the fractures and their cross-section variations. The obtained surface friction factor consistently varied between 1.04 and 1.65 in their investigations. To our knowledge, there is still no reliable literature on the estimation of the  $f$  factor in sand based eroded channels. Most of the studies that have investigated this effect focused on cross-section variations inside rocks. However, we believe that this same effect will influence the piping erosion channels and have therefore assumed a mid-range fracture surface characteristic factor of  $f = 1.345$  based on the results obtained from the study by Witherspoon et al. (1980).

## 2.2. Laminar flow transport equations

### 2.2.1. Incipient motion

The conceptualization of BEP combines the seepage flow in the dike foundation with the particle motion of the erosion process. The identification of incipient particle motion requires the definition of a critical transport condition. In sediment transport research, the use of the dimensionless Shields parameter  $\theta$  developed as a threshold erosion criterion. It compares the driving forces of particle motion (wall shear stress  $\tau_w$ ) with the resistance forces (particle weight):

$$\theta = \frac{\tau_w}{(\rho_p - \rho_f)gd} \tag{8}$$

In this,  $\rho_p$  represents the particle density and  $d$  the characteristic particle diameter. For laminar flow between parallel plates, the wall shear stress reads as

$$\tau_w = \frac{1}{2}\rho_f g \frac{\partial H}{\partial x} h \tag{9}$$

where  $\partial H/\partial x$  represents the local hydraulic gradient in the horizontal direction and  $h$  the pipe height. For the assessment of incipient motion, the Shields parameter is compared to the critical Shields parameter  $\theta_c$ . Table 1 presents four different expressions of this threshold which are all valid for laminar flow conditions. Only authors who also provide a relationship for the volumetric transport rate were considered.

Yalin and Karahan (1979) compiled data sets for incipient motion under laminar and turbulent flow conditions, including their own experimental data. Their analysis showed that both laminar and turbulent flows possess a different motion threshold curve, which,

**Table 2**  
Expressions for the dimensionless bedload transport rate in laminar flow.

Authors	Dimensionless bedload transport rate
Yalin (1963)	$q_b^* = 0.635s\sqrt{\theta} \left[ 1 - \frac{\ln(1+as)}{as} \right]$
Cheng (2004)	$q_b^* = 0.773Re_e^{1.78}\theta^{3.12}$
Charru et al. (2004)	$q_b^* = 0.025\theta(\theta - \theta_c) \frac{\sqrt{\rho_f(\rho_p - \rho_f)}\sqrt{gd^2}}{\eta_e}^3$
Ouriemi et al. (2009)	$q_b^* = \Phi_0 \frac{\theta_c}{12} \frac{\theta}{2\theta_c} \left( \frac{\theta^2}{\theta_c^2} + 1 \right) \frac{1}{5} \frac{\sqrt{\rho_f(\rho_p - \rho_f)}\sqrt{gd^2}}{\eta_e}^3$

eventually, led to an adaptation of the Shields diagram in the laminar flow regime. García-Flores and Maza-Alvarez (1997) fitted the laminar threshold curve of the critical Shields parameter into a practical equation:

$$\theta_c = \frac{0.1439}{d_*^{0.352}} + 0.0084e^{-\left(\frac{5.6243}{d_*}\right)^{9.21}}, \quad 0.2164 < d_* < 11.252 \quad (10)$$

Cheng (2004) derived the calculation of incipient sediment motion from Yalin et al. and correlated the critical Shields parameter with the dimensionless diameter

$$d_* = d \left( \frac{\rho_p - \rho_f}{\rho_f} \frac{g}{\nu^2} \right)^{\frac{1}{3}} \quad (11)$$

in which  $\nu$  represents the kinematic viscosity.

The experiments conducted by Charru et al. (2004) indicate a constant threshold of  $\theta_c = 0.12$  for the critical Shields parameter under saturated soil conditions.

Ouriemi et al. (2009) performed experiments under laminar flow conditions, in which they related the critical condition for incipient motion to the tangent of angle of repose  $\mu'$  and the volume fraction  $\Phi_0 = 1 - n$ . The experimental results of Cassar et al. (2005) imply a value of  $\mu' = 0.43$ , resulting in  $\theta_c = 0.135$  for a porosity of  $n = 0.37$ .

2.2.2. Sediment transport rate

Subsequent to the assessment of the incipient motion, a characterization of the transport rate is required. The bedload transport rate  $q_b$  is defined as the volume of eroded soil particles per unit width and within a unit time. Accordingly, the units are in  $m^2/s$ . Similar to the assessment of the incipient motion, the bedload transport rate will be expressed dimensionless:

$$q_b^* = \frac{q_b}{d \sqrt{\frac{\rho_p - \rho_f}{\rho_f}} gd} \quad (12)$$

Table 2 lists the expressions for the dimensionless bedload transport rate of the aforementioned authors.

In the expression put forward by Yalin, the parameters  $a$  and  $s$  are defined as follows:

$$a = 2.45 \frac{\sqrt{\theta}}{\left(\frac{\rho_p}{\rho_f}\right)^{0.4}} \quad (13)$$

$$s = \frac{\theta - \theta_c}{\theta_c} \quad (14)$$

Cheng stated that the sediment transport rate should not only rely on the Shields parameter, but should also consider the particle Reynolds number to account for viscous fluid effects. This becomes essential, especially for small particle Reynolds numbers of  $Re_* = \frac{u_* d}{\nu} < 70$  in which the shear velocity  $u_* = \sqrt{\tau_w/\rho_f}$ .

Charru et al. described the rolling, sliding, and bouncing of a mobile

**Table 3**  
Ranges of applicability.

Authors	Soil type	Charac. diameter [mm]	Density [kg/m <sup>3</sup> ]	Flow regime
IJkdijk 2009, Koelewijn et al. (2011)	IJkdijkzand 1&3	$d_{50} = 0.150$ $d_{50} = 0.209$	2650 2650	Laminar Laminar
Yalin 1963, Yalin (1963)	Gravel Barite Coal	$0.787 \leq D \leq 28.6$ $D = 5.21$ $D = 5.21$	2650 3220 250	Turbulent with laminar sublayer Turbulent & laminar
Yalin et al. 1979, Yalin and Karahan (1979)	Different sand types	$0.10 \leq D \leq 2.85$	2650	Laminar
Cheng (2004)	Quartz sand	$d_{mean} = 0.143$	2650	Laminar
Charru et al. (2004)	Acrylic bead	$d_{mean} = 0.580$	1180	Laminar
Ouriemi et al. (2009)	Glass Polystyrene PMMA	$D = 0.132$ $D = 0.538$ $0.132 \leq D \leq 0.193$	2490 1051 1177	Laminar Laminar Laminar

particle monolayer. Their description includes a viscous scaling of  $\sqrt{\rho_f(\rho_p - \rho_f)}\sqrt{gd^2}/\eta_e$ .

Ouriemi et al. applied a two-phase model with a continuum approach, in which the authors applied the same viscous scaling as Charru et al.

2.2.3. Ranges of applicability

Every transport equation is deduced and calibrated under specific flow and sediment conditions which restrict their applicability. The ranges of applicability of the aforementioned authors are presented in Table 3.

In IJkdijk Test 1 & 3, a fine IJkdijkzand with  $d_{50} = 0.150$  mm was used. In Test 2 a coarser IJkdijkzand with  $d_{50} = 0.212$  mm was used. The density of the IJkdijkzand particles was 2650 kg/m<sup>3</sup>.

In 1963, Yalin developed an expression for the dimensionless bedload transport rate. He adapted his analysis of sediment transport capacity to an experimental data set of Einstein. Einstein (1941). The sediment used in this study had a larger grain size ( $D$  represents the uniform grain diameter) than the IJkdijk soils which made it non applicable for our case. Yalin tested his model under turbulent flow conditions with a laminar sub-layer. However, in 2009, his modeling approach was additionally validated under pure laminar flow conditions (Parker, 2009). Furthermore, Malverti et al. (2008) reported that Yalin's dimensionless bedload transport equation was capable of describing sediment motion under both turbulent and laminar flow conditions. Alonso et al. (1981) studied nine different transport equations with respect to their applicability to shallow overland flows. He concluded that Yalin's bedload equation is especially valid for simulating transport rates of overland flows in a laminar flow regime. Before his formula was further validated under laminar flow conditions, Yalin himself had already developed the laminar onset criteria of sediment motion (Yalin and Karahan, 1979). This motion criterion was derived from experiments based on soils which were similar to the IJkdijkzand. Thus, Yalin (1963) and Yalin and Karahan (1979) provide a complete laminar transport model with onset criteria. Based on the presented evidence, we include Yalin's bedload transport equation in our study.

Cheng's transport model (Cheng, 2004) is derived from experimental observations of quartz sand grains from the Mersey estuary. The mean diameter  $d_{mean}$  of his experimental sample is similar to the  $d_{50}$  (median diameter) of the IJkdijkzand. We include this model in the present study as mean and median sand diameters are often similar in river sands originating from deltaic aquifers.

The transport model of Charru et al. (2004) was derived from experiments with acrylic beads of comparatively larger size and lower

density than sand. Accordingly, their transport equations are based on quite different sample characteristics and the IJkdijk soil is outside the range of applicability to these formulas. Nevertheless, the authors of this paper decided to include this sediment transport model in order to gain insight into the difference between the other three modeling approaches.

Ouriemi et al. (2009) conducted experiments using glass, polystyrene and PMMA, which all had a wide range of grain size and density distribution. Their transport equations, therefore, guarantee a broad applicability.

### 2.3. Exner's sediment mass conservation equation

The Exner's equation of sediment continuity aims to account for the changes in the soil bed due to fluctuations in the bedload transport rate (Paola and Voller, 2005). This equation will serve as an orientation for the determination of the pipe progression, and as a function of the eroded volume. The general Exner equation expresses that the bed level gradient  $\delta\eta/\delta t$  reacts proportionally to the bedload transport gradient  $\delta q_b/\delta x$ :

$$\frac{\delta\eta}{\delta t} = -\frac{1}{1-n} \frac{\delta q_b}{\delta x} \quad (15)$$

In the event of BEP, however, erosion occurs not only in a vertical  $\eta$ -direction but also in a horizontal  $x$ -direction. Instead of only considering the bed level gradient, the length gradient in the  $x$ -direction should also be included. The changes in height and length result in the area gradient  $\delta A/\delta t$ , which represents the eroded volume per unit width and within a unit time. The right side of Eq. (8) reflects the effect of porosity and describes the variation of the bedload transport rate. In the case of BEP, bedload is merely leaving the system and not entering it. Accordingly, the variation of the transport rate can be expressed as

$$-\frac{\delta q_b}{\delta x} = -\frac{q_{b,in} - q_{b,out}}{\delta x} = -\frac{0 - q_b}{\delta x} = \frac{q_b}{\delta x} \quad (16)$$

and the adapted Exner equation reads as follows:

$$\frac{\delta A}{\delta t} = \frac{1}{1-n} q_b \quad (17)$$

## 2.4. FEM implementation

### 2.4.1. Pipe height

The increased pipe area that forms due to the erosion process, leads to pipe lengthening  $\delta l$  and pipe deepening  $\delta h$ . As it is not possible to derive two variables ( $\delta l, \delta h$ ) from only considering the bedload transport rate, a second equation is required, relating the pipe height  $h$  to the pipe length  $l$ . There is little information available regarding the pipe height and in many cases the pipe height was set as a constant for the sake of simplicity (Zhou et al., 2012). However, it is important to consider that the pipe height is rising with the progression of the pipe due to an increasing erosion potential (Bersan et al., 2013). The field tests performed by Van Esch et al. (2013) reported that the pipe height can be described as a function of the particle diameter and varies from almost 0 grains, for very small pipes, to 10 grains, for fully developed pipes. Furthermore, the authors linked the pipe height to the pipe length by employing a square root expression. Based on these results, we define the average pipe height at every time step as the non-linear ratio between pipe length and maximum pipe length (dike width) as:

$$h(l) = 10d \sqrt{\frac{l}{l_{max}}} \quad (18)$$

### 2.4.2. Pipe progression

The eroded area  $A$  of the pipe (volume per unit width) is adjusted in

each time step in which erosion has been detected. This area can be calculated by means of an ordinary differential equation (ODE), relating  $A$  to its derivative with respect to the variable time (Eq. (10)). The exact expression of the ODE depends on the equation solver being used. The solver in the present study applies an order 1 backward differentiation formula scheme, corresponding to the backward Euler method. This is an implicit multistep method for solving initial value problems. Based on the calculation of the eroded area, which also corresponds to the product of pipe height and pipe length, it is then possible to determine the pipe length in time under consideration of Eq. (18). The pipe length is later used as an input variable for the change of porosity and permeability in space inside the predefined channel domain.

$$l = \left[ \frac{\sqrt{l_{max}}}{10d} \right]^{\frac{2}{3}} \quad (19)$$

The BEP process starts with the fluidization of the cohesionless soil at the exit point of the groundwater flow due to the upward component of the seepage force, also known as heave (Schweckendiek, 2014). We assume that heave has already occurred and, therefore, we have set the outlet location at the most downstream part of the dike toe. Our assumption is that an initial channel height of one grain diameter is the first step in the piping erosion process to develop. This initial channel height will result in an initial channel length of  $l_{max}/100$  according to Eq. (18). Based on these dimensions, the initial value for  $A$  in Exner's equation (Eq. (10)) reads as  $A_{initial} = h_{initial} * l_{initial} = \frac{d_{50} * l_{max}}{100}$ .

### 2.4.3. Numerical solvers and mesh configurations

The finite element method implemented in COMSOL Multiphysics is the Galerkin method (AB, 2019). For the specific case of Darcy's law, no stabilization was required. COMSOL calculates the independent variable of pressure  $p$  in combination with the variable  $A$  in Exner's equation. This eroded area  $A$  employs an additional global ordinary differential equation (ODE) at every step. This time dependence is solved using an implicit backward differentiation formula (BDF), which allows for the determination of the exact required time step according to the amount of transported soil constrained from each sediment transport model. The rest of the system is solved with the direct algorithm MULTifrontal Massively Parallel sparse direct Solver (MUMPS) (AB, 2019). The present model uses a refined triangular mesh optimized for the solution of Darcy's equation. In a first step, the complete erosion channel length is meshed with an element size of  $10d_{50} * 10d_{50}$ . Secondly, the aquifer domain is meshed with an element growth function of 1.1, starting from the closest element in the channel grid. The pressure variables are discretized based on a quadratic Lagrange shape order. Further solver configurations and discretization schemes can be found in the COMSOL Multiphysics reference manual for porous media models (AB, 2019).

## 3. The IJkdijk

The IJkdijk (Dutch for 'calibration dike') is a research program for the investigation of dike failure mechanisms and sensor technologies. During the experiment in 2009 (Koelewijn et al., 2011), four different tests were conducted to study the BEP process. Tests 1–3 are chosen as models in our numerical approach, as the monitored pore pressures in Test 4 were affected by a malfunctioning drainage system (Koelewijn et al., 2014). For each test, a 15 m wide, 3.5 m high clay dike was built on a 2.8 m to 3 m deep sandy foundation, surrounded by an impermeable basin. The dikes were gradually loaded on the upstream side and a downstream water level of 10 cm was maintained to ensure a full saturation of the subsoil. In order to match the value of the hydraulic loading with the hydraulic head, the water level on the downstream side was set as the zero datum.

The low permeability of the dike material allows us to determine that the seepage flow inside the dike is negligible compared to the groundwater flow in the sandy aquifer. Consequently, the modeling approach

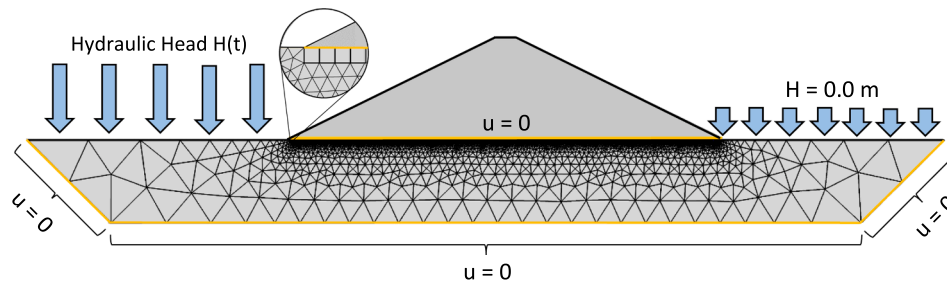


Fig. 2. IJkdijk cross-section with mesh and boundary conditions.

Table 4  
Parameters of the IJkdijk Tests 1–3.

Parameters	Symbol	Value	Unit
Intrinsic permeability (Test 1 & 3)	$\kappa$	$1.01 \cdot 10^{-11}$	$m^2$
Intrinsic permeability (Test 2)	$\kappa$	$1.76 \cdot 10^{-11}$	$m^2$
Charac. diameter (Test 1 & 3)	$d$	$1.5 \cdot 10^{-4}$	$m$
Charac. diameter (Test 2)	$d$	$2.09 \cdot 10^{-4}$	$m$
Porosity (Test 1 & 3)	$n$	0.4	–
Porosity (Test 2)	$n$	0.37	–
Geom. cross-section factor (Test 1,2 & 3)	$\beta$	96	–
Hydraulic Tortuosity factor (Test 1 & 3)	$T_h$	1.49	–
Hydraulic Tortuosity factor (Test 2)	$T_h$	2.23	–
Cross-section variation factor (Test 1,2 & 3)	$f$	1.345	–
Cubic law adjustment factor (Test 1 & 3)	$\alpha$	192	–
Cubic law adjustment factor (Test 2)	$\alpha$	288	–
Kinematic viscosity (12 °C)	$\nu$	$1.236 \cdot 10^{-6}$	$m^2/s$
Intrinsic particle density	$\rho_p$	2650	$kg/m^3$
Intrinsic fluid density	$\rho_f$	1000	$kg/m^3$
Particle compressibility	$\chi_p$	$1 \cdot 10^{-8}$	$1/Pa$
Fluid compressibility	$\chi_f$	0	$1/Pa$

defines the dike as impermeable and only the seepage flow in the dike foundation is modeled. Fig. 2 represents the physical model set-up of the IJkdijk test configurations and contains the mesh elements in addition to the boundary conditions. The inlet boundary condition and the outlet boundary condition are depicted by the blue arrows. The remaining yellow borders in the diagram describe the interface between the aquifer

and the dike, as well as the limitations of the subsoil, and they are accompanied by no-flow boundary conditions.

Table 4 lists the material properties, which are based on the following assumptions:

- The aquifer is homogeneous and isotropic.
- The characteristic particle diameter can be represented by the median particle diameter  $d = d_{50}$ .
- The pore water was defined as incompressible since the volumetric deformations are marginal compared to variations in the pore volume.
- The compressibility of the aquifer was set to  $\chi_p = 1 \cdot 10^{-8} 1/Pa$  for compacted sand.

The determination of the cubic law adjustment factor  $\alpha$  for Test 1 & 3 and Test 2 is described in Appendix A.

### 3.1. Pore pressure and pipe length developments

With each test configuration (Tests 1–3), the number and locations of the piezometers vary. In Test 1, 64 piezometers were installed in four rows with a longitudinal distance of approx. 1.0 m. In Test 2 & 3, additional piezometers were installed, resulting in 120 and 112 sensors, respectively. Fig. 3 illustrates the sensor matrices in the dike foundations, which were installed just below the interface between the dike and the aquifer. The sensors selected for the evaluation of the pore pressure measurements are highlighted in green.

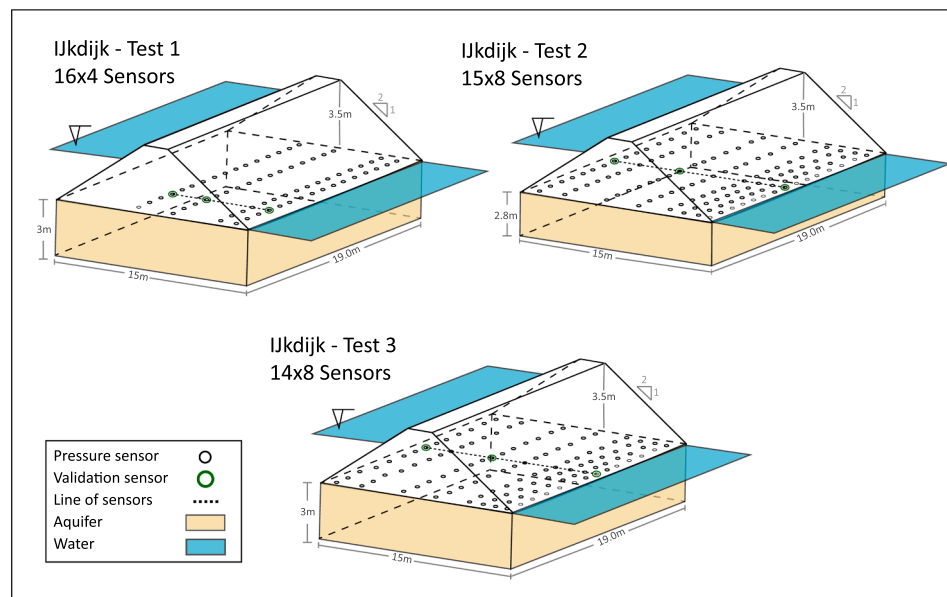


Fig. 3. Dike geometry and sensor locations.

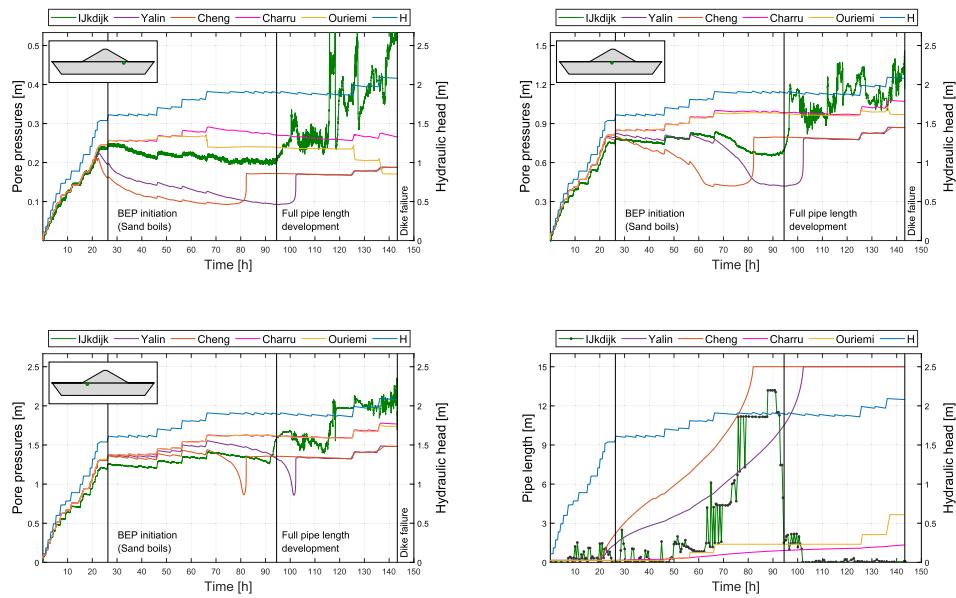


Fig. 4. Numerical and experimental pore pressure & pipe length development of IJkdijk Test 2 with three BEP transition characteristics: BEP initiation (Sand boils), Full pipe length development, Dike failure.

3.1.1. Analysis and numerical modeling of IJkdijk Test 2

Fig. 4 compares the experimental pore pressure and pipe length developments of IJkdijk Test 2 with the numerical simulations. The pore pressure developments will be discussed at three specific piezometer locations: at the upstream and downstream side as well as in the center of the dike. The pore pressure measurements of the experiment are visualized by the green line, while the violet, orange, pink and yellow lines represent the numerically obtained pore pressures, applying the sediment transport equations of Yalin et al. ("Yalin"), Cheng, Charru et al. ("Charru") and Ouriemi et al. ("Ouriemi"). The hydraulic head is depicted by the blue line and the black vertical lines describe the visual observations during the experiment (Koelewijn et al., 2011).

At the beginning of Test 2, the hydraulic head increased gradually, leading to a proportional rise in pore water pressures at all three sensor locations. After 26 h, sand boils occurred, which indicate the initiation of BEP, since larger amounts of sand were transported to the

downstream exit point. BEP initiation results in an anomalous pore pressure decrease, as the erosion channel is an area of high permeability and thus of low hydraulic resistance. Most of the energy, therefore, dissipates in the less permeable zone in front of the pipe. Initially, when the pipes are still relatively small, they have little influence on the surrounding pressure field. Accordingly, the pressure drop was first recognizable at the downstream sensor.

The graph in the bottom right-hand corner describes the pipe length development. The reconstructed pipe length of the IJkdijk experiment indicates that small pipes were created exceedingly early on, but collapsed quite frequently, and that stable pipes were only formed after 50 h. The graph also includes the pipe length developments of the numerical models. Based on the sediment transport equations of Yalin and Cheng, BEP initiated after approx. 20 h. Applying the sediment transport equations of Charru and Ouriemi, the erosion process commenced after approx. 24 h and 46 h, respectively.

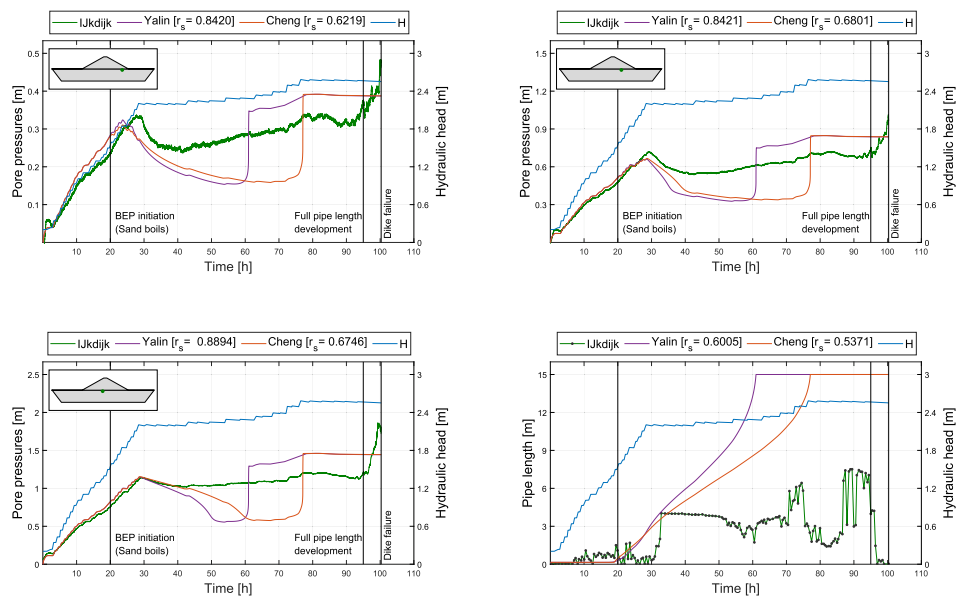


Fig. 5. Numerical and experimental pore pressure & pipe length development of IJkdijk Test 1 with three BEP transition characteristics: BEP initiation (Sand boils), Full pipe length development, Dike failure.

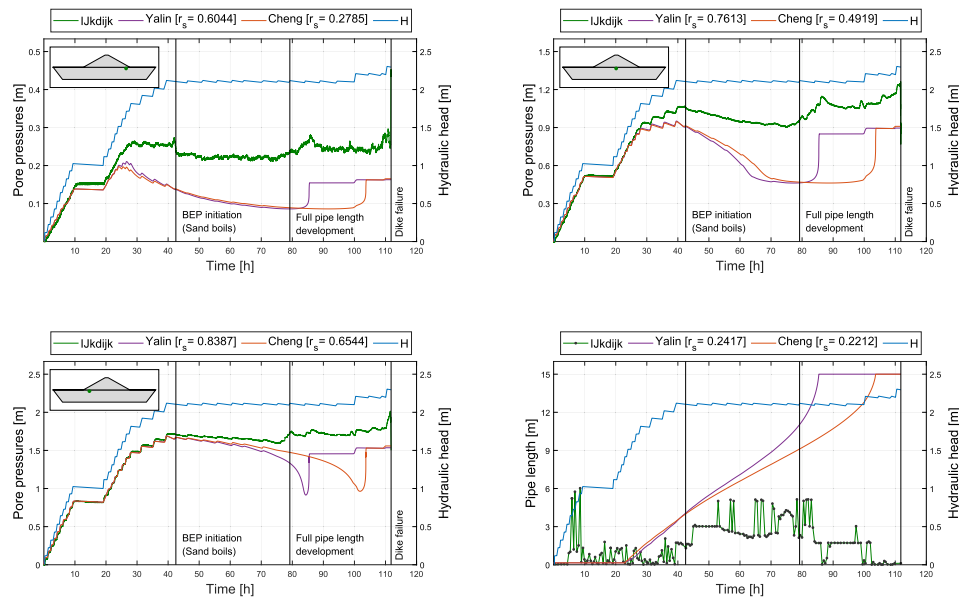


Fig. 6. Numerical and experimental pore pressure & pipe length development of IJkdijk Test 3 with three BEP transition characteristics: BEP initiation (Sand boils), Full pipe length development, Dike failure.

Subsequent to the initiation of BEP, the pipe progressed and increased its influence on the surrounding pressure field. The pipe approached the piezometer in the center of the dike (top right-hand graph) and just before the pipe reached this sensor location, a pore pressure drop is visible. Shortly after, the pressure stabilized, which may reflect that the piping process was stagnating, but in this case, it indicates that the erosion channel surpassed the sensor location. A first pressure stabilization is visible in Cheng's modeling approach after approx. 65 h. The pipe length development shows that, at this time, the pipe had progressed up to half the dike width. The pressure stabilization can also be observed in the IJkdijk experiment and in the model based on Yalin. In Charru's and Ouriemi's modeling approaches, the pipes remained very small during the time of the experiment, resulting in insignificant influences on the sensors remote from the downstream side.

After 94.5 h in the experiment, the pipe reached the upstream side, and the widening process of the pipe began. The pipe length development illustrates that, in the models based on Charru's and Ouriemi's sediment equations, the pipe did not reach the full pipe length within the time of the experiment. In Cheng's and Yalin's modeling approaches, the pipe was fully developed after 82 h and 102 h, respectively. As soon as the pipe reached the upstream side, the pore pressures increased rapidly at all sensor locations. The pipe was then connected to the water reservoir and the water flowed directly into the pipe. Instead of losing pressure head in the soil in front of the pipe, the pore pressure inside the pipe decreased linearly towards the downstream side. Even though the dike collapsed at the end of the experiment, the reconstructed pipe length of the IJkdijk experiment never reaches the full length of 15 m (dike width). The results of the monitoring system are limited and show how difficult it is to accurately monitor piping. However, the general development of the pipe length is recognizable. Yalin's and Cheng's modeling approaches produce comparable results, and their pore pressure readings also behave similarly to the monitored pore pressures of the IJkdijk experiment. Charru's and Ouriemi's modeling approaches were not capable of simulating the full development of the pipe length. Accordingly, the following analysis will focus on Yalin's and Cheng's sediment transport modeling approaches.

### 3.1.2. Analysis and numerical modeling of IJkdijk Test 1 & 3

In order to better understand the applicability of Yalin's and Cheng's sediment transport equation to the description of the BEP process, their

performances were examined in Test 1 & 3, which had the same dike configuration. Fig. 5 contains the pore pressure and pipe length developments of IJkdijk Test 1. During the experiment, the first sand boils were detected after 20 h and in the two selected numerical modeling approaches, BEP initiated at almost the same time. The pressure drop, which indicates the start of the erosion process, occurred simultaneously at all sensor positions. In Yalin's modeling approach, the pipe reached the upstream side after 61 h and in Cheng's modeling approach after 77 h. In the experiment, the penetration into the water reservoir was detected only after 95 h, shortly before the actual failure of the dike.

For a better assessment of the two different modeling approaches in terms of their pressure distribution and pipe length development, we have chosen the Spearman's rank correlation coefficient. This coefficient is a non-parametric measure for correlation, which determines the degree of dependence between two variables. Due to its ranking nature, more importance is given to the fact that two functions follow the same trend rather than their magnitude. This choice is further explained in this paper's discussion section. A perfect Spearman's rank correlation results in a value of  $r_s = 1$  and no correlation leads to values close to zero. In Yalin's modeling approach, the experimental and numerical pore pressure developments show a high rank correlation and the Spearman's coefficient ranges from  $r_s = 0.84$  to  $r_s = 0.89$ . In comparison, the correlation values in Cheng's model are lower and range from  $r_s = 0.62$  to  $r_s = 0.68$ . In both modeling approaches, the numerical pipe length developments show a weak correlation to the reconstructed pipe lengths of the experiment, as the experimental results fail to accurately represent the actual progression of the erosion process.

Fig. 6 illustrates the pore pressure and pipe length developments of IJkdijk Test 3. This time, the first sand boils were not observed until 42.5 h. However, when looking at the pipe length development, it can be seen that frequently collapsed pipes had already formed at an earlier stage. Additionally, the monitored pore pressures at the downstream sensor location (top left graph) stagnated after 25 h, although the hydraulic head continued to increase. This indicates that the erosion process may have begun even before the first sand boils were visible. In the two selected numerical models, BEP started after approx. 23 h. The pipe then continued to progress until it reached the upstream side. This could be observed in the experiment after 79 h. In the numerical model based on Yalin's sediment transport equations, the pipe reached the upstream side only a few hours later. In Cheng's modeling approach, however, the pipe progression required more time. The determination of the rank

**Table 5**  
Critical Shields parameter, Delta Shields parameter and bedload transport rate for a given  $\theta = 0.15$  in IJkdijk Test 2.

Model	$\theta_c [-]$	$\Delta\theta [-]$	$q_b [m^2/s]$
Yalin and Karahan (1979), Yalin (1963)	0.084	0.066	$3.56E-7$
Cheng (2004)	0.094	0.056	$2.90E-7$
Charru et al. (2004)	0.120	0.030	$5.45E-9$
Ouriemi et al. (2009)	0.135	0.015	$3.52E-7$

correlation, likewise, indicates that Yalin’s model better reproduced the experimental observations. Once more, the reconstructed pipe lengths are not capable of reflecting the actual erosion course, resulting in weak correlations for the pipe length developments.

**4. Discussion of numerical results**

The proposed numerical solution combines Darcy groundwater flow in the aquifer with sediment transport equations for laminar flow inside the erosion channel. It enables us to simulate the main initial events of BEP: initiation, progression, and full pipe length development. The widening of the erosion channel and the eventual dike failure are not included in this study. The numerically obtained pore water pressure distributions were compared with the ones recorded by piezometers in the IJkdijk experiment. We were able to relate the time of occurrence of the initial BEP events to pore pressure transitions.

The erosion process starts as soon as the Shields parameter within the predefined erosion channel exceeds the critical Shields parameter, which varies depending on each respective sediment transport model. As an explanatory example, we have chosen a Shields parameter of  $\theta_{given} = 0.15$ , which corresponds to the maximum Shields parameter in Ouriemi’s model. Table 5 presents the difference between the given Shields parameter and each of the author’s critical Shields parameter ( $\Delta\theta = \theta_{given} - \theta_c$ ). Based on this specific  $\theta_{given}$  the final column shows the calculated bedload transport rates of each of the respective authors. This

allows us to compare the difference in the onset and the transport magnitude as the same Shields parameter is applied in each model. Note, that this value occurs at different moments in time depending the chosen model.

Fig. 7 depicts the results of Table 5 and the listed parameters are marked as points in the graphs. The left-hand graph depicts the time-dependent Delta Shields parameter. As soon as  $\Delta\theta > 0$ , the erosion process commences. The relatively low critical Shields parameters of Yalin and Cheng led to an earlier BEP initiation than in the piping models based on Charru and Ouriemi. During the erosion process it is possible for the Delta Shields parameter to return into the negative, causing the transport rate to drop to zero and the erosion to stagnate. Continuous erosion can only be found in Yalin’s model. Nevertheless, in Cheng’s model the pipe length development is progressing faster as his transport rate for Shields parameters just above the critical threshold is higher than Yalin’s transport rate. This effect is reversed at high Shields parameters, like  $\theta_{given} = 0.15$ . According to the final column of Table 5, Charru’s approach yields an erosion rate, which is two orders of magnitude lower than the other models’ erosion rates. This results in a very weak pipe progression. Accordingly, his transport equations are not applicable to the description of the BEP process as its computed bedload transport rate is too low. This was expected from Charru’s model due to the large differences between the IJkdijkzand and the acrylic particles used for deriving his laminar flow transport model.

Ouriemi’s transport equation model yields similar rates as Yalin’s and Cheng’s models, but in Ouriemi’s modeling approach, the high critical threshold of  $\theta_c = 0.135$  poses a major barrier for the numerical model to identify incipient sediment motion and the erosion process mainly stagnated. However, as soon as erosion occurred, a high transport rate could be observed. This led to a very staggered pipe length development, resulting in a pipe length of about four meters at the end of the experiment. The calculation of  $\theta_c$  in Ouriemi’s model highly depends on the choice of the angle of repose, which can be set to  $\mu' = 0.43$  at laminar flow conditions for small glass beads ( $D = 0.112 \text{ mm}$ ,  $\rho_p = 2470 \text{ kg/m}^3$ ) (Cassar et al., 2005). However, we believe that the angle of repose of the sand particles during the BEP process differs from the

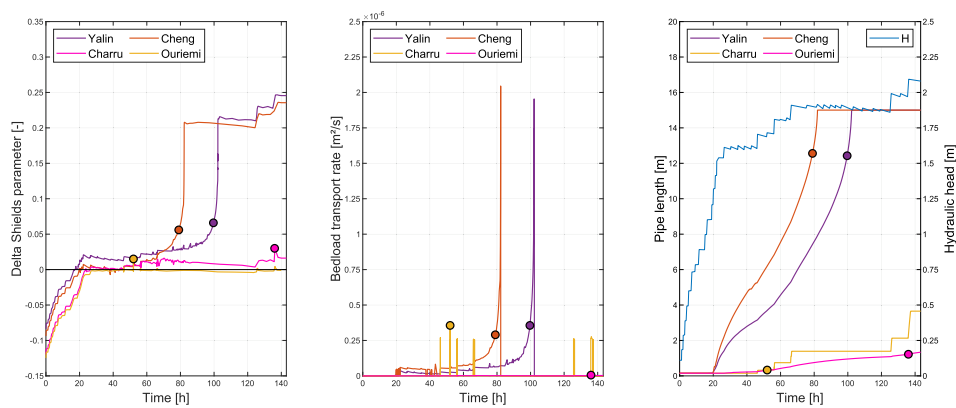


**Fig. 7.** Delta Shields parameter, bedload transport rate and pipe length development for the IJkdijk Test 2. Points over lines represent  $\Delta\theta, q_b, l$  values for moments in time in which  $\theta_{given} = 0.15$ .

**Table 6**  
Comparison of the numerical results to the experimental observations for all three test configurations.

Model	BEP characteristic	Test 1	Test 2	Test 3	Average ratio	Average $\bar{r}_c$
		Time: ratio	Time: ratio	Time: ratio		
IJkdijk (Koelewijn et al., 2011)	Initiation	20 h: -	26 h: -	42.5 h: -	-	-
Yalin and Karahan (1979), Yalin (1963)	Full pipe length	95 h: -	94.5 h: -	79 h: -	0,78	0,80
	Initiation	17,5 h: 0,92	19 h: 0,73	22 h: 0,52		
Cheng (2004)	Full pipe length	61 h: 0,64	102 h: 0,93	85.5 h: 0,92	0,78	0,57
	Initiation	19 h: 0,95	20 h: 0,77	23 h: 0,54		
	Full pipe length	77 h: 0,81	82 h: 0,87	103.5 h: 0,76		

proposed value of 0.43. Accordingly, Ouriemi's sediment transport equations should not be applied to describe particle motion during piping erosion before further research on the angle of repose is conducted.

The complete pipe length development could only be simulated in Yalin's and Cheng's modeling approaches. Therefore, the performance of their sediment transport equations was additionally investigated in Test 1 & 3. Both approaches provided satisfactory results. Table 6 compares the results of Yalin's and Cheng's numerical simulation approaches with the experimental IJkdijk observations (top row). The first line of each row reflects the moment in which first sand boils were discovered, i.e. when BEP initiated. The second line describes the time required for the pipe to fully develop and to penetrate into the upstream water reservoir. The second row presents the results of the numerical model based on Yalin's sediment transport equations and its percentage accordance (ratio) with the experimental IJkdijk observations. In Test 1, the piping process in Yalin's model started after 17.5 h, while in the IJkdijk experiment piping initiation was determined after 20 h. This leads to a high time ratio of the numerical result to the experimental observation. In Test 3, however, sand boils were only discovered after 42.5 h, even though the dike configuration was identical to that in Test 1 with similar hydraulic loads. Consequently, individual experimental test results should be regarded with caution. The numerical simulation, on the other hand, produces very comparable results in both Test 1 & 3. The six different time ratios have been averaged to show that the visual observations of the experiment could be matched to the numerical simulation with an accuracy of 78%. The third row depicts the results of the numerical model based on Cheng's sediment transport equation. His modeling approach predicts the pipe progression with a similar averaged time ratio of 78%.

The comparison of the numerical results to the experimental observations shows that both models deliver promising results of capturing the spatial-temporal erosion process. To allow further conclusions to be drawn about the performance of the modeling approaches, the Spearman's rank correlation between the experimental and simulated pore pressures was calculated. As shown in the analysis of IJkdijk Test 1 & 3, the pore pressure development of Yalin's model has a much higher rank correlation to the experimental observations than Cheng's model. In the final column of Table 6, the averaged Spearman's rank correlation coefficient  $\bar{r}_s$  is specified, which was determined by averaging all six pore pressure rank coefficients of Test 1 & 3. We decided to focus only on the pore pressure coefficients, as in the IJkdijk experiment the development of the frequently collapsing erosion channels could not be reproduced appropriately. The reconstructed pipe lengths were estimated from a mathematical fitted function and not from actual observations or measurements during the experiment (Sellmeijer et al., 2011). Consequently, a comparison with our numerical pipe length development is of little relevance. Pore pressure transitions are a major indicator of erosion and, accordingly, the averaged Spearman's rank correlation coefficient is crucial for the evaluation of the erosion models. Yalin's model delivers a coefficient of  $\bar{r}_s = 0.80$ , which is significantly greater than in Cheng's model, where  $\bar{r}_s = 0.57$ .

This raises the question why Yalin's model better reflects the pore pressure development during the piping process, whereas both, Yalin's and Cheng's model produced an equal time ratio of 78%. This is due to the fact that the time ratio is based on the time information derived from the visual observations during the experiment, which are subject to human error. Visually identifying the time of BEP initiation as well as the time of full pipe length development is considerably difficult. In Test 1, for example, the full pipe length development was only discovered after 95 h, shortly before the dike collapsed. In this case it is probable that a pipe outlet on the upstream side remained unnoticed for a significant amount of time. The Monitoring of pore pressures, in contrast, records any changes in the subsurface and reacts more sensitively to fuzzy conditions such as full pipe length development of frequently collapsing pipe structures. Even though, in Test 1, Cheng's model has a

higher time ratio, Yalin's model better reflects the changes in pore pressure. Since the averaged time ratio of both modeling approaches is identical, we employed the additional analysis of the Spearman rank coefficient. This results in a recommendation that further research should follow the modeling approach based on Yalin's sediment transport equations for dike configurations similar to those of the IJkdijk experiment.

However, this conclusion has to be approached with caution. The presented BEP model strongly depends on the fictitious permeability derived from the cubic law. The cubic law approximation allows us to solve both porous and non-porous media with only one single numerical solution. While this is the main added value of the presented approach, it is still expected that a coupled numerical solution of Darcy's law and Navier–Stokes equations provides better results and requires fewer correcting factors, decreasing the uncertainty in this implementation. Nevertheless, Bersan et al. (2013) proved the cubic law to be a reasonable approximation by comparing the fictitious permeability method to the ideal solution of the Navier–Stokes equations.

In order to account for deviations from the idealized smooth, straight, and parallel-plated channel model, we introduced the  $\alpha$  adjustment factor of the fictitious permeability. The results of this study strongly depend on the three friction effects ( $\beta$ ,  $T$  and  $f$ ). Therefore, we recognize that these correction factors require more thorough laboratory investigation under controlled conditions. Furthermore, it is of paramount importance to gain deeper insights into the erosive capacity of the BEP process in order to better determine the values of  $\beta$ ,  $T_h$  and  $f$ . In order to ensure a valid comparison between the different transport models, the same  $\alpha$  adjustment factor was used per test configuration. We believe that the friction effects should always be determined based on the sand properties and not on their expected improvement in the model performance. Consequently, the main calibration factor of the model is the determination of the channel height (Eq. (18)).

It should be noted that in Test 1 & 3, the dike configurations were the same, but the pipe progressions differed significantly. Therefore, further studies of the IJkdijk experiment should reconsider the assumption of the homogeneous aquifer. The implementation of heterogeneities in the subsoil would certainly enhance the validity of the present model. In combination with an extension to a 3D model and a search algorithm, the numerical model would be capable of simulating a meandering and branching pipe development. The 3D model would also permit to laterally shift the erosion path, thus reducing the effect of the BEP process on the pore pressures at the sensor locations. In our 2D simulation, piping erosion takes place directly below the sensors, which results in much more pronounced pore pressure transitions than in the IJkdijk experiment.

Our numerical model is based on the premise that the selected sediment transport equations for the erosion on river beds can directly be applied to piping research. Therefore, it has to be verified that the flow inside the erosion channel remains laminar during the entire simulation. The critical Reynolds number, describing the transition from laminar to turbulent flow, corresponds to  $Re_c = 1400$  for infinitely wide pipes (Fox and McDonald, 1994). Appendix B shows the temporal development of the Reynolds number for each modeling approach for all three IJkdijk tests at the pipe outlet. The downstream pipe outlet is the location with the highest flow velocities and Reynolds numbers. The maximum obtained Reynolds number in the numerical simulation was  $Re = 310$ , which is far below the critical Reynolds number. We were able to confirm the assumption of laminar flow inside the erosion channel, which can be explained by the small hydraulic diameter of the pipe and the limited velocities under the hydraulic loads applied to dikes.

The proposed transient piping model not only provides a new approach for the numerical modeling of BEP, it also allows for an easy identification of pore pressure transitions due to pipe progression. Hence, our method provides a basis for the evaluation under which conditions piping monitoring would be sensible. At present, research in

this area is limited, since monitoring elongated structures with punctual pore water pressure measurements requires an extremely high number of sensors. In order to keep the monitoring system economical, research is currently being carried out using fiber optic cable-based sensors, acting as distributed pressure sensors.

## 5. Conclusion

The proposed numerical formulation of the BEP process couples existing sediment transport equations for laminar flow with a Darcy groundwater solution and Exner's mass conservation equation. The inclusion of criteria for incipient particle motion, as well as the linkage of the bedload transport rate to the pipe progression, enables us to build a stable time-dependent piping model. Four different modeling approaches for laminar flow were compared with respect to their pore pressure and pipe length developments. The transport models based on Charru et al. and Ouriemi et al. provide unsatisfactory results for their implementation into a piping model. However, we were able to demonstrate the applicability of the sediment transport equations of Yalin et al. and Cheng to with the description of particle motion during the BEP process. The numerical models based on their sediment transport equations reproduce the spatial-temporal erosion process of the

IJkdijk experiment with an accuracy of 78%. According to the evaluation of the Spearman's rank correlation between the experimental and simulated pore pressure developments, we recommend applying the sediment transport equations of Yalin and Karahan (1979, 1963) for the simulation of BEP in sand types similar to those used in the IJkdijk experiment.

## Declaration of Competing Interest

The authors declare that they have no known competing financial interests or personal relationships that could have appeared to influence the work reported in this paper.

## Acknowledgements

The authors acknowledge the European Commission (Horizon 2020) and the Netherlands Organisation for Scientific Research (NWO) for financial support within the Water JPI Call and the WaterWork2014 Cofunded Call for project DOMINO ALWWW.2014.1 and the Dutch Foundation for applied water research (STOWA) for the additional financial support.

## Appendix A

Limited literature and data exists regarding tortuosity values in the context of piping research. Van Beek (2015) is one of the few authors who published experimental findings, visualizing pipe progression. In order to ascertain which of these experiments should be used to determine the tortuosity values of the IJkdijk test configurations, we compared the coefficient of uniformity and the hydraulic conductivity of the soils in the experiments to those of the IJkdijk sand, see Table 7.

In order to determine the tortuosity of IJkdijk Test 1 & 3 we included an experiment by Silvis (1991), who conducted large-scale experiments on piping erosion in the Delta Flume. In this experiment the soil was covered by a transparent layer for the sake of observing the piping erosion pathway. Experiment T3 had a seepage length of 6 m and the Marsdiep sand had similar hydraulic properties to the IJkdijk sand in Test 1 & 3. In order to determine the hydraulic tortuosity, we measured the geometric tortuosity (see Fig. 8), and obtained a hydraulic tortuosity of:

$$T_{h,1\&3} = \left(\frac{6.71m}{5.50m}\right)^2 = 1.49 \quad (20)$$

In establishing the tortuosity value of the pipe in IJkdijk Test 2, we examined a specific experiment by Van Beek (2015), who conducted various small-scale experiments on BEP. In her graphs, the pipe contours were drawn manually to show the piping erosion pathway, see Fig. 9. Experiment O163 had a seepage length of 300 mm and the Oostelijke sand had similar hydraulic properties to the IJkdijk sand in Test 2. The analysis of this experiment yields a hydraulic tortuosity of:

$$T_{h,2} = \left(\frac{0.363m}{0.243m}\right)^2 = 2.23 \quad (21)$$

The Oostelijke sand caused a higher tortuosity value, which can be explained by the higher coefficient of uniformity and the higher hydraulic permeability in this test configuration (Espinoza et al., 2015). Finally, the cubic law adjustment factors of all IJkdijk Test configurations are calculated:

$$\alpha_{1\&3} = \beta T_{h,1\&3} f = 96 * 1.49 * 1.345 = 192 \quad (22)$$

$$\alpha_2 = \beta T_{h,2} f = 96 * 2.23 * 1.345 = 288 \quad (23)$$

**Table 7**

Soil properties of the selected experiments.

Experiment	Coefficient of uniformity [-]	Hydraulic conductivity [m <sup>2</sup> /s]
IJkdijk Test 1 & 3 (Koelewijn et al., 2014)	1.6	8.0E-05
Delta Flume T3 (Silvis, 1991)	1.6	5.1E-05
IJkdijk Test 2 (Koelewijn et al., 2014)	1.8	1.4E-04
O163 (Van Beek, 2015)	2.1	1.3E-04

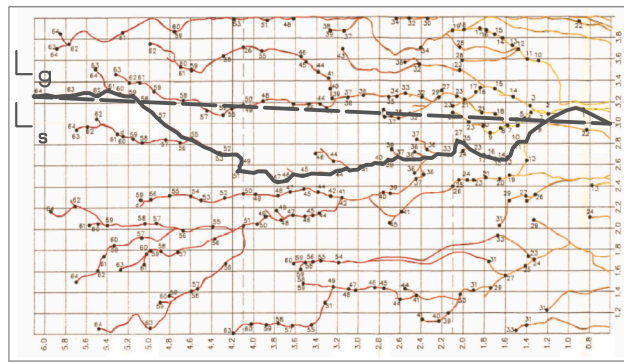


Fig. 8. Determination of the geometric tortuosity of IJkdijk Test1&3 (Van Beek, 2015).

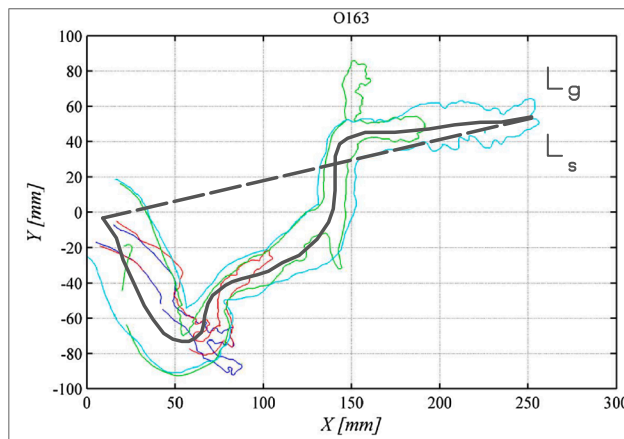


Fig. 9. Determination of the geometric tortuosity of IJkdijk Test 2 (Van Beek, 2015).

Appendix B

Fig. 10.

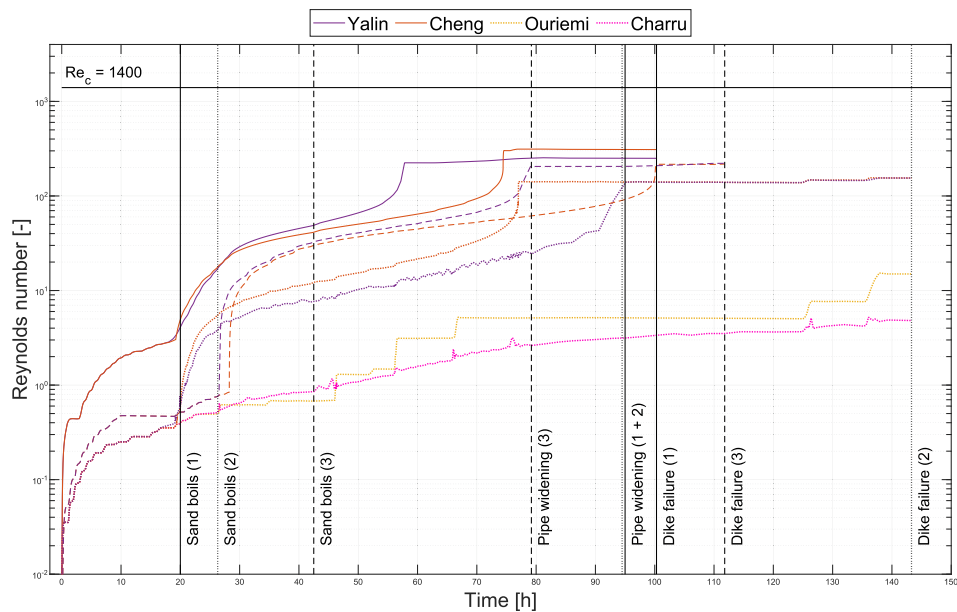


Fig. 10. Development of the Reynolds number for all four different modeling approaches for all three IJkdijk tests.

## References

- C. AB, 2019. Comsol multiphysics v. 5.4. reference manual, COMSOL AB, Stockholm, Sweden, 1084.
- Aguilar-López, J.P., Warmink, J.J., Schielen, R.M.J., Hulscher, S.J., 2018. Piping erosion safety assessment of flood defences founded over sewer pipes. *Eur. J. Environ. Civil Eng.* 22 (6), 707–735.
- Alonso, C., Neibling, W., Foster, G., 1981. Estimating sediment transport capacity in watershed modeling. *Trans. ASAE* 24 (5), 1211–1220.
- Bear, J., 1975. *Dynamics of fluids in porous media*. Courier Corporation.
- Bersan, S., Jommi, C., Koelewijn, A., Simonini, P., 2013. Applicability of the fracture flow interface to the analysis of piping in granular material. In: *Proc., COMSOL Conference, Rotterdam, The Netherlands, 2013*, pp. 23–25.
- Bligh, W., 1910. Dams, barrages and weirs on porous foundations. *Eng. News* 64 (26), 708–710.
- Bui, T.-A., Gelet, R., Marot, D., 2019. Modelling of internal erosion based on mixture theory: General framework and a case study of soil suffusion. *Int. J. Numer. Anal. Meth. Geomech.* 43 (15), 2407–2430.
- Cassar, C., Nicolas, M., Pouliquen, O., 2005. Submarine granular flows down inclined planes. *Phys. Fluids* 17 (10), 103301.
- Charru, F., Mouilleron, H., Eiff, O., 2004. Erosion and deposition of particles on a bed sheared by a viscous flow. *J. Fluid Mech.* 519, 55–80.
- Cheng, N.-S., 2004. Analysis of bedload transport in laminar flows. *Adv. Water Resources* 27 (9), 937–942.
- Clennell, M.B., 1997. Tortuosity: a guide through the maze. *Geol. Soc., London, Special Publicat.* 122 (1), 299–344.
- Cook, A., Myer, L., Cook, N., Doyle, F., 1990. The effects of tortuosity on flow through a natural fracture.
- Danka, J., Zhang, L., 2015. Dike failure mechanisms and breaching parameters. *J. Geotech. Geoenviron. Eng.* 141 (9), 04015039.
- De Vries, G., Koelewijn, A., Hopman, V., 2010. Ijkdijk full scale underseepage erosion (piping) test: Evaluation of innovative sensor technology. In: *Scour and Erosion*, pp. 649–657.
- De Wit, J., Sellmeijer, J., Penning, A., 1981. Laboratory testing on piping. *Soil Mech. Found. Eng.* 517–520.
- Einstein, H.A., 1941. Formulas for the transportation of bed load. *Trans. ASCE* 561–597.
- El Shamy, U., Aydin, F., 2008. Multiscale modeling of flood-induced piping in river levees. *J. Geotech. Geoenviron. Eng.* 134 (9), 1385–1398.
- El Shamy, U., Zeghal, M., 2005. Coupled continuum-discrete model for saturated granular soils. *J. Eng. Mech.* 131 (4), 413–426.
- Elsworth, D., Goodman, R., 1986. Characterization of rock fissure hydraulic conductivity using idealized wall roughness profiles. In: *International Journal of Rock Mechanics and Mining Sciences & Geomechanics Abstracts, Vol. 23*, Elsevier, 1986, pp. 233–243.
- Espinoza, M., Sundén, B., Andersson, M., Yuan, J., 2015. Analysis of porosity and tortuosity in a 2d selected region of solid oxide fuel cell cathode using the lattice boltzmann method. *ECS Trans.* 65 (1), 59–73.
- Fox, R.W., McDonald, A.T., 1994. *Introduction to fluid mechanics*. John Wiley & Sons Inc, New York.
- Fujisawa, K., Murakami, A., Nishimura, S.-I., 2010. Numerical analysis of the erosion and the transport of fine particles within soils leading to the piping phenomenon. *Soils Found.* 50 (4), 471–482.
- García-Flores, M., Maza-Alvarez, J., 1997. *Inicio de movimiento y acorazamiento, Manual de Ingeniería de Ríos, Series del Instituto de Ingeniería* 592.
- Ge, S., 1997. A governing equation for fluid flow in rough fractures. *Water Resour. Res.* 33 (1), 53–61.
- Ghanbarian, B., Hunt, A.G., Ewing, R.P., Sahimi, M., 2013. Tortuosity in porous media: a critical review. *Soil Sci. Soc. Am. J.* 77 (5), 1461–1477.
- Griffith, W., 1914. The stability of weir foundations on sand and soil subject to hydrostatic pressure. (abridged). In: *Minutes of the Proceedings of the Institution of Civil Engineers, Vol. 197, Thomas Telford-ICE Virtual Library, 1914*, pp. 221–232.
- Hanses, U.K., 1985. *Zur Mechanik der Entwicklung von Erosionskanälen in geschichtetem Untergrund unter Stauanlagen*. Universitätsbibliothek der TU Berlin.
- Jianhua, Y., 1998. Fe modelling of seepage in embankment soils with piping zone. *Chin. J. Rock Mech. Eng.* 17 (6), 679–686.
- Koelewijn, A., Pals, N., Sas, M., Zomer, W., 2011. Ijkdijk piping experiment: Validatie van sensor-en meettechnologie voor detectie van optreden van piping in waterkeringen. *Stowa rapport 2010–26 PIW; isbn 978.90. 5773.485. 4*.
- Koelewijn, A., De Vries, G., Van Lottum, H., Förster, U., Van Beek, V., Bezuijen, A., 2014. Full-scale testing of piping prevention measures: Three tests at the ijkdijk. *Proc. Phys. Model. Geotech.* 2, 891–897.
- Lachouette, D., Golay, F., Bonelli, S., 2008. One-dimensional modeling of piping flow erosion. *Comptes Rendus Mécanique* 336 (9), 731–736.
- Lane, E.W., 1935. Security from under seepage masonry dams on earth foundations. *Trans. ASCE* 100, 1234–1351.
- Li, X., Jiang, Z., Min, C., 2019. Quantitative study of the geometrical and hydraulic characteristics of a single rock fracture. *Energies* 12 (14), 2796.
- Lominé, F., Scholtes, L., Sibille, L., Poullain, P., 2013. Modeling of fluid–solid interaction in granular media with coupled lattice boltzmann/discrete element methods: application to piping erosion. *Int. J. Numer. Anal. Meth. Geomech.* 37 (6), 577–596.
- Malverti, L., Lajeunesse, E., Métivier, F., 2008. Small is beautiful: Upscaling from microscale laminar to natural turbulent rivers. *J. Geophys. Res.: Earth Surf.* 113 (F4).
- Mühlhaus, H., Gross, L., Scheuermann, A., 2015. Sand erosion as an internal boundary value problem. *Acta Geotech.* 10 (3), 333–342.
- Müller-Kirchenbauer, H., Rankl, M., Schlötzer, C., 1993. Mechanism for regressive erosion beneath dams and barrages, in: *Proceedings of the First International Conference on Filters in Geotechnical and Hydraulic Engineering, Balkema*, pp. 369–376.
- Muzychka, Y., Yovanovich, M., 2009. Pressure drop in laminar developing flow in noncircular ducts: A scaling and modeling approach. *J. Fluids Eng.* 131 (11), 111105.
- Ojha, C., Singh, V., Adrian, D., 2003. Determination of critical head in soil piping. *J. Hydraul. Eng.* 129 (7), 511–518.
- Ouriemi, M., Aussillous, P., Guazzelli, E., 2009. Sediment dynamics. part 1. bed-load transport by laminar shearing flows. *J. Fluid Mech.* 636, 295–319.
- Paola, C., Voller, V.R., 2005. A generalized exner equation for sediment mass balance. *J. Geophys. Res.: Earth Surf.* 110 (F4).
- Papamichos, E., Vardoulakis, I., 2005. Sand erosion with a porosity diffusion law. *Comput. Geotech.* 32 (1), 47–58.
- Parker, G., 2009. Ms yalin's contribution to bedload transport in rivers: 46 years of hindsight. *Canad. J. Civil Eng.* 36 (10), 1579–1586.
- Qiu-ling, Y., Liu-qian, D., Dong-ya, S., Chang-jun, L., Qi-yi, Z., 2007. Experimental studies on piping in single-and two-stratum dike foundations [j]. *Water Resour. Hydropower Eng.*, vol. 2.
- Robbins, B., 2016. Numerical modeling of backward erosion piping. *Appl. Numer. Model. Geomech.* 551–558.
- Rotunno, A.F., Callari, C., Froio, F., 2019. A finite element method for localized erosion in porous media with applications to backward piping in levees. *Int. J. Numer. Anal. Meth. Geomech.* 43 (1), 293–316.
- Schmertmann, J.H., 2000. The no-filter factor of safety against piping through sands. In: *Judgment and innovation: the heritage and future of the geotechnical engineering profession, 2000*, pp. 65–132.
- Schweckendiek, T., 2014. On reducing piping uncertainties: A bayesian decision approach.
- Sellmeijer, J.B., 1988. On the mechanism of piping under impervious structures. ph.d. thesis.
- Sellmeijer, J., Koenders, M., 1991. A mathematical model for piping. *Appl. Math. Model.* 15 (11–12), 646–651.
- Sellmeijer, H., de la Cruz, J.L., van Beek, V.M., Knoeff, H., 2011. Fine-tuning of the backward erosion piping model through small-scale, medium-scale and ijkdijk experiments. *Eur. J. Environ. Civil Eng.* 15 (8), 1139–1154.
- Silvis, F., 1991. *Verificatie piping model: proeven in de deltagoot, Delft, the Netherlands: Grondmechanica Delft (in Dutch)*.
- Snow, D.T., 1965. A parallel plate model of fractured permeable media. ph.d. thesis.
- Stavropoulou, M., Papanastasiou, P., Vardoulakis, I., 1998. Coupled wellbore erosion and stability analysis. *Int. J. Numer. Anal. Methods Geomech.* 22 (9), 749–769.
- Terzaghi, K., Peck, R.B., Mesri, G., 1996. *Soil mechanics in engineering practice*. John Wiley & Sons.
- Tran, D.K., Prime, N., Froio, F., Callari, C., Vincens, E., 2017. Numerical modelling of backward front propagation in piping erosion by dem-lbm coupling. *Eur. J. Environ. Civil Eng.* 21 (7–8), 960–987.
- Van Beek, V., 2015. Backward erosion piping: initiation and progression.
- van Beek, V.M., Robbins, B.A., Hoffmans, G.J., Bezuijen, A., van Rijn, L.C., 2019. Use of incipient motion data for backward erosion piping models. *Int. J. Sediment Res.*
- Vandenboer, K., Van Beek, V., Bezuijen, A., 2013. 3d fem simulation of groundwater flow during backward erosion piping. In: *5th International Young Geotechnical Engineers' Conference (YGEC 2013), Vol. 2, IOS Press, 2013*, pp. 301–304.
- Van Esch, J., Sellmeijer, J., Stolle, D., 2013. Modeling transient groundwater flow and piping under dikes and dams. In: *Proceedings, Third International Symposium on Computational Geomechanics (ComGeo III)*. Taylor & Francis, London, 2013.
- Wang, D.-Y., Fu, X.-D., Jie, Y.-X., Dong, W.-J., Hu, D., 2014. Simulation of pipe progression in a levee foundation with coupled seepage and pipe flow domains. *Soils Found.* 54 (5), 974–984.
- Wang, L., Cardenas, M.B., Slottke, D.T., Ketcham, R.A., Sharp Jr, J.M., 2015. Modification of the local cubic law of fracture flow for weak inertia, tortuosity, and roughness. *Water Resour. Res.* 51 (4), 2064–2080.
- Witherspoon, P.A., Wang, J.S., Iwai, K., Gale, J.E., 1980. Validity of cubic law for fluid flow in a deformable rock fracture. *Water Resour. Res.* 16 (6), 1016–1024.
- Xiao, W., Xia, C., Wei, W., Bian, Y., 2013. Combined effect of tortuosity and surface roughness on estimation of flow rate through a single rough joint. *J. Geophys. Eng.* 10 (4), 045015.
- Yalin, M.S., 1963. An expression for bed-load transportation. *J. Hydraul. Divis.* 89 (3), 221–250.
- Yalin, M.S., Karahan, E., 1979. Inception of sediment transport. *J. Hydraul. Divis.* 105 (11), 1433–1443.
- Zhang, X., Wong, H., Leo, C.J., Bui, T.A., Wang, J., Sun, W., Huang, Z., 2013. A thermodynamics-based model on the internal erosion of earth structures. *Geotech. Geol. Eng.* 31 (2), 479–492.
- Zhou, X.-J., Jie, Y.-X., Li, G.-X., 2012. Numerical simulation of the developing course of piping. *Comput. Geotech.* 44, 104–108.